Sum Frequency Generation Microscopy Study of Cellulose Fibers

HOANG CHI HIEU, NGUYEN ANH TUAN, HONGYAN LI, YOSHIHIRO MIYAUCHI, and GORO MIZUTANI*

School of Materials Science, Japan Advanced Institute of Science and Technology, 1-1 Asahidai, Nomi, Ishikawa 923-1292, Japan (H.C.H., N.A.T., H.L., H.M., G.M.); Japan Science and Technology Agency, Core Research for Evolutional Science and Technology, 5-3 Sanban-cho, Chiyoda-ku, Tokyo 102-0075, Japan (N.A.T., H.L., Y.M., G.M.); and Faculty of Physics, Hanoi University of Science, 334 Nguyen Trai, Thanh Xuan, Hanoi 10000, Vietnam (H.C.H.)

Sum frequency generation (SFG) microscopy images of cotton cellulose fibers were observed at the infrared wavenumber of ~ 2945 cm^{-1} and with a spatial resolution of 2 μm. Domains of different cellulose microfibril bunches were observed and they showed different second-order nonlinear responses. The intensity of the peak of the asymmetric CH_2 stretching mode at 2945 cm^{-1} depended strongly on the orientation of the electric fields of the incident visible and infrared light with respect to the cellulose fiber axis. The second-order nonlinear susceptibility arising from the chirality in the cellulose structure was found to be dominant. The SFG of the cross section of the cellulose fiber was relatively weak and showed a different spectrum from that measured from the side of the fiber axis.

Index Headings: **Sum frequency generation; SFG; Microscope; Infrared spectroscopy; IR spectroscopy; Cellulose; Chirality.**

INTRODUCTION

Nonlinear optical microscopy has developed remarkably in recent decades. The technique gives images of considerable contrast[1] that are invisible using conventional microscopy. Regarding second-order nonlinear microscopy, there have been many second harmonic generation (SHG) microscope studies.[1–4] Another important second-order nonlinear microscope is the sum frequency generation (SFG) microscope. Due to its selectivity for molecular vibrational modes, it is a powerful tool for probing biological molecules due to its sensitivity for chirality in the biomaterials[5–9] such as DNA[6,7] and protein.[8,9] Miyauchi et al. used SFG microscopy to observe in vivo a water plant *Chara fibrosa* and detected amylopectin selectively in it.[5] Motivated by these studies, we are trying to give a further demonstration of SFG microscopy for biological studies.

We chose cellulose as the sample for demonstrating our measurement. In samples like the water plant observed by Miyauchi et al.,[5] the dominant material after amylopectin and amylose is cellulose. Cellulose is a linear homopolymer composed of (1–4)-β-glucopyranose and is the most abundant polymer in nature. Arrangement and orientation of cellulose fibrils are important for the individual plant cell and the development of the plant as a whole.[2] Thus, the observation of this material by a new microscopic method is expected to offer useful information.

Cellulose found in nature is cellulose I and occurs primarily in two crystalline allomorphs, I_α and I_β. In cotton and wood, cellulose I_β is the more abundant. Cellulose I_β chains are arranged in a monoclinic $P2_1$ symmetry.[10] This crystalline structure belongs to chiral space group, a non-centrosymmetric group, and the functional groups of the glucopyranose units are located in non-centrosymmetric orders.[11] Therefore, SFG can be active in most cellulose I_β. The CH_2 groups are oriented in the same direction in one microfibril of cellulose[10–12] as seen in Fig. 1. The chirality of crystalline cellulose microfibrils is mainly presented at the hydroxymethyl groups. Well-ordered microfibril domains of cellulose fiber make a high chirality. The crystalline domain has a width of several nanometers and a length of tens of nanometers.[10] The physical properties of polymorphs, such as crystal modulus and tensile strength, are different from each other due to the different bunching and orientation of the highly ordered crystalline microfibrils. Thus, microscopic study of the orientation of microfibrils in cellulose should be important because the properties of products consisting of cellulose are affected by the orientation in industries such as papermaking and textile production.

Using conventional Raman spectroscopy, Atalla et al. reported evidence of molecular orientation of single native cellulose fibers in 1980, and many researchers followed him.[13–15] Zimmerley et al. measured coherent anti-Stokes Raman scattering (CARS) and Raman spectra and images of dried and hydrated cellulose fibers in cotton and rayon from 2800 cm^{-1} to 3000 cm^{-1}. The peak at 2890 cm^{-1} depended strongly on the orientation of the fiber, while the peak at 2965 cm^{-1} did not.[14] In the case of cellulose microfiber orientation of *picea abies* studied by Raman microscopy by Gierlinger et al.,[15] the images taken at the peak at 2890 cm^{-1} did not have high contrast of orientation dependence.

The optical second-order nonlinear response is expected to be more sensitive to orientation anisotropy of cellulose fibers than Raman scattering. The orientation dependence of the SHG response of native cellulose fiber in cotton and in *Valonia* has been studied using SHG microscopy.[15–17] On the other hand, Cox et al. argued that cellulose does not seem to generate strong SHG signal due to the low asymmetry of the polyglucan chain.[2] In addition, SHG cannot detect the direction of CH_2 or CH bonds of cellulose molecules.

The work by Barnettte et al. reporting the first SFG spectra of cellulose[18] appeared while the present paper was being prepared. They reported on the SFG spectra of model cellulose sample pressed into a pellet in the wavenumber range from 1000 cm^{-1} to 3800 cm^{-1}. They reported on the skeletal modes of cellulose near 1000 cm^{-1} and C–H asymmetric vibration modes near 2900 cm^{-1} and the O–H vibration near 3300 cm^{-1}. However, this is the average response of position in the sample and orientation of the microfibrils. The chiral SFG response should depend on the orientation of the cellulose microfibril axis due to variation in the contribution of chiral and achiral susceptibility elements. Thus, microscopic measurement of SFG signal from well-ordered cellulose fiber is expected. In our

Received 20 June 2011; accepted 5 August 2011
* Author to whom correspondence should be sent. E-mail: mizutani@jaist.ac.jp.
DOI: 10.1366/11-06388

0003-7028/11/6511-1254$2.00/0

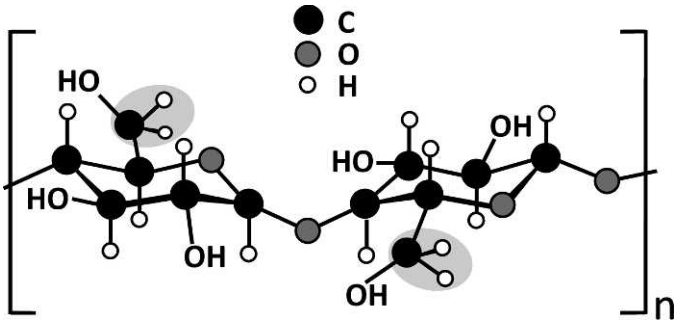

FIG. 1. Chemical structure of a cellulose polymer. Here n is the number of cellobiose units (also called degree of polymerization) of cellulose. Two CH_2 groups are highlighted by the gray circular background.

previous work we constructed a confocal SFG microscope system.[19] By utilizing this optics we can measure the local SFG response of cellulose fibers with a spatial resolution of 2 μm. This would be a very good tool to investigate microfibrils in the cellulose fibers.

In this paper, we used our sum frequency microscope to investigate cotton cellulose fibers, in order to probe chirality and orientation of the cellulose microfibril domains in μm scale. The SFG intensity at frequency $\omega_{SFG} = \omega_{vis} + \omega_{IR}$ is given as:[20]

$$I(\omega_{SFG}) \propto |\chi^{(2)}_{eff}|^2 I(\omega_{vis}) I(\omega_{IR}) \quad (1a)$$

Here, $I(\omega_{vis})$ and $I(\omega_{IR})$are the intensities of the output fields, $\chi^{(2)}_{eff}$ is the effective second-order nonlinear susceptibility defined as:

$$\chi^{(2)}_{eff} = [L(\omega_{SFG} \cdot \hat{e}_{SFG})] \cdot \chi^{(2)} : [L(\omega_{vis} \cdot \hat{e}_{vis})][L(\omega_{IR} \cdot \hat{e}_{IR})] \quad (1b)$$

Here $L(\omega_i)$ and $\hat{e}_i$ are the tensorial Fresnel factor and unit vector of the electric field at ω_i, respectively.[20]

For monoclinic $P2_1$ symmetry of cellulose crystallite, there are 13 nonvanishing elements of second-order nonlinear susceptibility as:[21]

$$\chi^{(2)}_{yxz}, \chi^{(2)}_{zxy}, \chi^{(2)}_{yzx}, \chi^{(2)}_{zyx}, \chi^{(2)}_{yyx}, \chi^{(2)}_{zzx}, \chi^{(2)}_{yxy}, \chi^{(2)}_{zxz}, \chi^{(2)}_{xyy}, \chi^{(2)}_{xzz}, \chi^{(2)}_{xzy}, \chi^{(2)}_{xyz}, \chi^{(2)}_{xxx} \quad (2a)$$

Here we choose the crystalline axis to coincide with the laboratory coordinate ($\hat{x}$, $\hat{y}$, $\hat{z}$) with twofold axis parallel to $\hat{x}$. We assume that the microfibril bunch axis is parallel to $\hat{x}$, and thus y and z are equivalent to each other. Hence, the susceptibility elements can be expressed as:

$$\chi^{(2)}_{yxz} = \chi^{(2)}_{zxy}, \chi^{(2)}_{yzx} = \chi^{(2)}_{zyx}, \chi^{(2)}_{yyx} = \chi^{(2)}_{zzx}, \chi^{(2)}_{yxy} = \chi^{(2)}_{zxz}, \chi^{(2)}_{xyy} = \chi^{(2)}_{xzz}, \chi^{(2)}_{xzy} = \chi^{(2)}_{xyz}, \chi^{(2)}_{xxx} \quad (2b)$$

Table I shows bands in the vibrational spectrum of cellulose and assignments according to the literature. Due to overlap of bands in the CH region, it is difficult to assign bands from the Raman data. Thus, there is debate over assignment in the CH region. Barnette et al. reported that the CH stretching mode is silent in SFG spectra of cellulose; they assign the peaks at 2850 cm^{-1} and 2945 cm^{-1} to symmetric and asymmetric stretching modes, respectively.

TABLE I. Peak wavenumber of bands in the CH region and assignment according to the literature.[a]

Wavenumber (cm^{-1})	Raman (Atalla et al.[22])	FT Raman (Fischer et al.[23])	Raman, CARS (Zimmerley et al.[14])	SFG (Barnette et al.[18])	SFG (this work)
2850				$\nu_s(CH_2)$	$\nu_s(CH_2)$
2890	$\nu(CH)$	$\nu(CH)$	$\nu_s(CH_2)$		
2945	$\nu_a(CH_2)$			$\nu_a(CH_2)$	$\nu_a(CH_2)$ or FR
2965	$\nu_a(CH_2)$	$\nu_a(CH_2)$	$\nu(CH)$		$\nu_a(CH_2)$

[a] $\nu(CH)$: CH stretching mode; $\nu_s(CH_2)$: symmetric CH_2 stretching mode; $\nu_a(CH_2)$: asymmetric CH_2 stretching mode; FR: Fermi resonance.

EXPERIMENTAL

Filter Papers (Advantec MFS, Inc.) with 100% cotton linter cellulose I were used as samples for the experiment. The paper filter (thickness of 70 μm) was cut in small pieces and stuck on a glass plate 15 mm × 15 mm to prevent movement. The experimental setup for the SFG confocal microscope measurement is shown in Fig. 2 and is very similar to that used in our previous study.[19] As a visible light source at wavelength of 532 nm we used a frequency-doubled output from a mode-locked Nd:YAG laser operating at repetition a rate of 10 Hz. As a wavelength-tunable infrared light source we used an output with wavelength of ~ 3.4 μm and band width < 6 cm^{-1} from an optical parametric generator and amplifier system (OPG/OPA) driven by the same YAG laser. We used half-wave plates to change the polarization of the infrared and visible beams.

The visible light passed through a dichroic mirror (DCM: Semrock, FF506-Di02) and was focused on the sample by a 20× objective lens (numerical aperture, NA = 0.45) with a spot size on the sample of 2–3 μm. The infrared beam was focused on the sample by a CaF_2 lens of $f = 200$ mm with spot sizes on the sample of 50–100 μm. The visible light and infrared light reach the sample at incident angles of 0° and 50°, respectively. The reflective angle of the SFG signal was estimated as ~10°. The pulse energy of the infrared light was 50 μJ, while that of

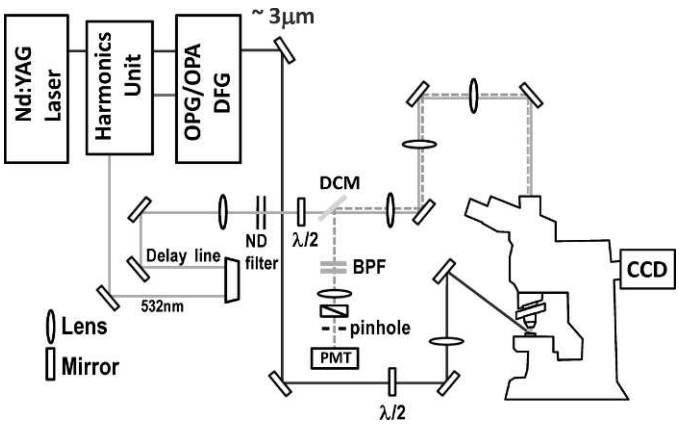

FIG. 2. Experimental setup for the SFG measurements of cellulose fibers. OPG/OPA DFG represents the optical parametric generator/amplifier and difference frequency generator. PMT represents a photomultiplier. BPF represents the bandpass filter. DCM represents the dichroic mirror. CCD camera represents the charge-coupled device camera. ND filter represents the neutral density filters. λ/2 represents the half-wave plate.

the visible light was less than 1 μJ. A delay line was used to adjust the temporary overlap of the infrared and visible pulses. We used a red diode laser beam propagating collinearly with the infrared laser beam to optimize the overlap of the visible and infrared beam spots on the sample with the naked eye.

The imaging optics was a commercial microscope (Nikon Eclipse: LV100D). The SFG light from the sample was collected by the objective lens and a tube lens of focal length $f = 200$ mm in the microscope optics. It then became a parallel beam with a lens of $f = 200$ mm and propagated back as long as 1800 mm on the same optical path as the incident beam. The SFG light was then reflected by the DCM, passed through band pass filters (OPL FF01-472/30-25 and THORLABS FB460-10), a lens with focal length $f = 100$ mm, and a pinhole with diameter of 400 μm and finally detected by a photomultiplier. The infrared pulse energies were monitored by a photodiode and the SFG intensity was normalized. The SFG spectra of the cellulose fibers were obtained from 2800 cm^{-1} to 3050 cm^{-1} with 5 cm^{-1} steps. The accumulation for each point was 200 laser shots.

For the SFG images of cellulose fibers, the samples were put on a piezo stage and moved on the horizontal x–y plane in steps of 0.5 or 1 μm. The scanned area was 100 μm × 100 μm. It took about 90 minutes to obtain one SFG image. The experiments were carried out in air at room temperature of 21 °C.

RESULTS AND DISCUSSION

Sum Frequency Spectroscopy. Figures 3a through 3c show SFG spectra from the cotton cellulose fiber. The optical configuration is schematically shown in the inset of each panel. For later convenience we name the plane including the two beam paths the incident plane. For Fig. 3a the cellulose fiber axis is perpendicular to the incident plane, while for Fig. 3b the cellulose fiber is in the incident plane. We define the angle α as the angle between the electric field of the visible light and the axis of the cellulose fiber, and the angle β as the angle between the projection of the electric field of the infrared light on the x–y plane and the fiber axis. Here the x, y, and z directions are defined in Figs. 3a, 3b, and 3c and the x direction is parallel to the fiber axis for all three cases.

In Figs. 3a and 3b the solid and dashed curves are the SFG signal at $\alpha = 0°$ and 90°, respectively. The angle β is 90° for Fig. 3a and 0° for Fig. 3b. For Fig. 3c the cellulose fiber axis is parallel to the axis of the collection optics and the path of the incident visible laser beam. In Fig. 3c both visible and infrared electric fields are in the incident plane. The spectrum for the visible electric field perpendicular to the incident plane is almost the same as that in Fig. 3c and is not shown. In the measurement of Figs. 3a to 3c the SFG polarization was not specified. The SFG intensity for $\alpha = \beta = 0°$ and with the infrared wavenumber 2945 cm^{-1} polarized in the y direction was around five times as large as that polarized in the x direction. Namely, the emitted SFG light field was polarized mostly perpendicular to the incident visible field.

The spectra in Figs. 3a and 3b show prominent peaks at 2945 cm^{-1} and shoulders around 2965 cm^{-1}. This result is consistent with the SFG spectrum of a pellet of model cellulose Avicel® PH-101 reported by Barnette et al.[18] The SFG spectra in Figs. 3a and 3b depend strongly on the polarization of the visible light relative to the orientation of the cellulose fiber axis. Namely, the SFG intensity at $\alpha = 0°$ is significantly stronger

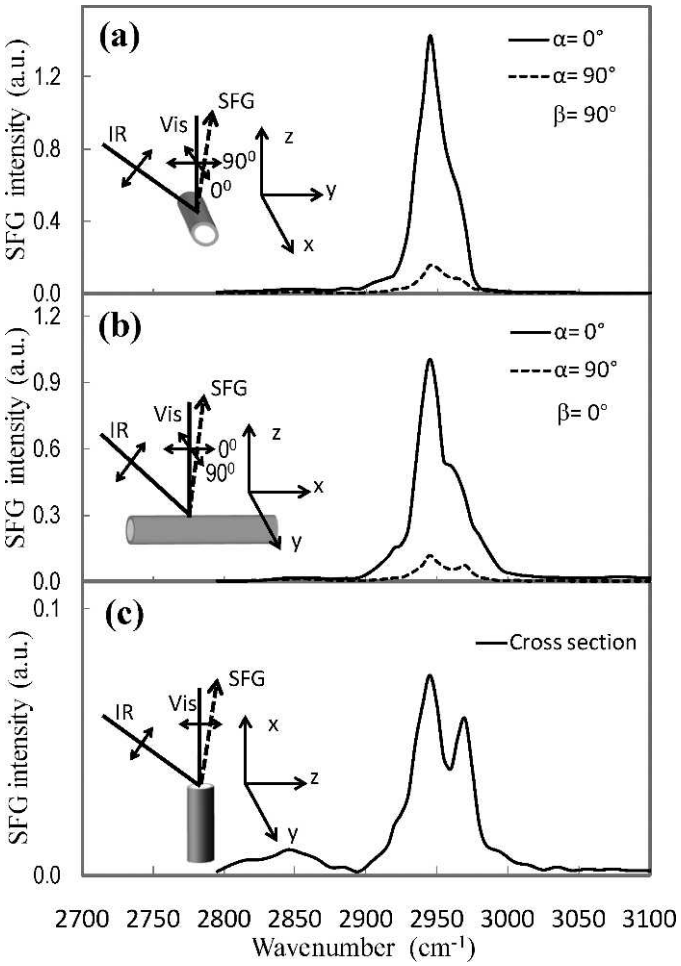

FIG. 3. Sum frequency spectra of cellulose fiber with (**a**) polarizations of infrared and visible lights the same and (**b**) polarization of the visible light perpendicular to that of the infrared light, and (**c**) of the cross section of the fiber.

than that at $\alpha = 90°$. Barnette et al. did not report polarization dependence of the SFG signal because they used a pressed pellet as the sample.

According to Barnette and co-workers, the CH stretching mode is silent in the SFG spectra of cellulose due to high symmetry of CH groups in the cellulose molecule.[18] This is the reason the most intense peak at ~ 2890 cm^{-1} assigned to the CH stretching mode in the Raman data did not appear in the SFG spectra. Therefore, we assign both the peak at 2945 cm^{-1} and the shoulder at 2965 cm^{-1} to asymmetric CH_2 stretching modes according to some of the proposals in the literature.[18,22,23] The two peaks may correspond to the opposite relative phase of the asymmetric stretching vibrations of two CH_2 groups in one cellobiose unit as can be seen in Fig. 1, caused by different dipole moment directions. There is also a possibility that the peak at 2945 cm^{-1} can be attributed to the Fermi resonance of CH_2 groups. In either assignment the asymmetric vibration of CH_2 groups is important in the SFG signal. SFG microscopy can selectively visualize the CH_2 group in the cellulose fiber. In this context, SFG microscopy is more beneficial than SHG microscopy.[2]

Figure 3c shows a typical SFG spectrum of the cross section of a cellulose fiber. The SFG spectrum does not depend on the visible light polarization and thus only the spectrum is shown

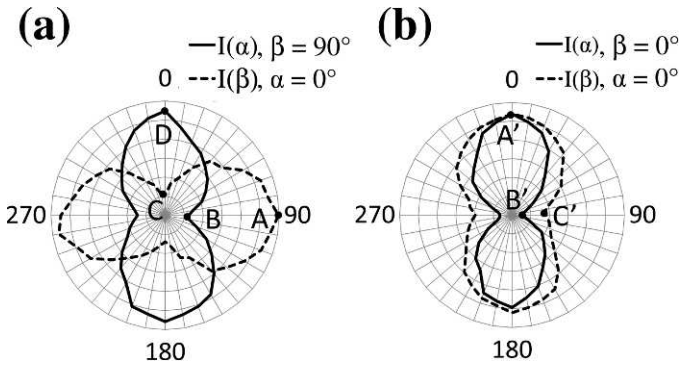

FIG. 4. The SFG intensity of the cellulose fiber as a function of α and β with the fiber axis (**a**) perpendicular and (**b**) parallel to the incident plane. The solid curve represents the SFG intensity as a function of α with β = 90° for (a) and β = 0° for (b). The dashed curve represents the SFG intensity as a function of β with α = 0°.

for both the visible and infrared light polarizations parallel to the incident plane. The spectrum shows clear double peaks at 2945 cm^{-1} and at 2970 cm^{-1} and a small peak at 2850 cm^{-1}. According to the discussion above, the peaks at 2945 cm^{-1} and at 2970 cm^{-1} are assigned to the asymmetric stretching modes of CH_2 groups. The intensity ratio of the 2970 cm^{-1} peak to that of 2945 cm^{-1} is different among Figs. 3a, 3b, and 3c. Here we notice that the polarization of the visible light is perpendicular to the fiber axis for the dashed spectra in Figs. 3a and 3b and for that in Fig. 3c. This is the reason for the similar spectral shapes in these three configurations. According to Barnette et al.[18] the peak at 2850 cm^{-1} is assigned to the symmetric CH_2 stretching mode.

Figure 4 shows the SFG intensity at 2945 cm^{-1} as a function of the angles α and β with the fiber axis perpendicular (Fig. 4a) and parallel (Fig. 4b) to the incident plane. With respect to the incident plane the cellulose fiber axes for Figs. 4a and 4b are set in configurations similar to those for Figs. 3a and 3b, respectively. The solid curve is the SFG intensity as a function of α with the infrared polarization at β = 90° for Fig. 4a and β = 0° for Fig. 4b. The dashed curve represents the SFG intensity as a function of β with the visible light polarization at α = 0° in both Figs. 4a and 4b. The probed position on the cellulose fiber sample was chosen to be the same for the two cases. For both solid curves in Figs. 4a and 4b, the SFG intensity is at maximum when the visible polarization direction α is either 0° or 180°. On the other hand, for dashed curves in Fig. 4 the SFG intensity is at maximum for the infrared polarization β = 90° or 270° in Fig. 4a, while it is at maximum for β = 0° or 180° in Fig. 4b.

Here we try to guess the dominant nonlinear susceptibility element contributing to the SFG intensity in Figs. 3 and 4. For the polarization combination all,s,p (non-specified SFG, *s*-polarized visible, and *p*-polarized infrared) and the angles α = 0°, β = 90 °, corresponding to the solid spectra in Fig. 3a and point A in the dashed curve in Fig. 4a, the effective nonlinear susceptibility can be given in the laboratory coordinate as [20, 24]:

$$\chi^{(2)}_{1.\mathrm{all,s,p}} = -L_{yy}(\omega_{\mathrm{SFG}})L_{xx}(\omega_{\mathrm{vis}})L_{yy}(\omega_{\mathrm{IR}}) \cdot \chi^{(2)}_{yxy}\cos\theta + L_{yy}(\omega_{\mathrm{SFG}})L_{xx}(\omega_{\mathrm{vis}})L_{zz}(\omega_{\mathrm{IR}}) \cdot \chi^{(2)}_{yxz}\sin\theta \qquad (3a)$$

Here, $L_{\xi\xi}(\omega_i)$ is the Fresnel factor in the ξ direction at ω_i. The subscript 1 in the effective nonlinear susceptibility indicates the configuration in the inset of Fig. 3a. θ (=50°) is the incident angle of the IR beam. We assumed that the reflective angle of the SFG beam is approximately equal to zero. We also used the fact that the emitted SFG light field was polarized mostly perpendicular to the incident visible field. We confirmed in a separate experiment that the linear images of the fibers depended very weakly on the input polarization. Thus, the Fresnel factors of three waves in each term of Eq. 3a can be grouped into one factor as *L*. Then the SFG intensity at A is

$$I_{\mathrm{A}} \propto |\chi^{(2)}_{1.\mathrm{all,s,p}}/L|^2 = |-\chi^{(2)}_{yxy}\cos\theta + \chi^{(2)}_{yxz}\sin\theta|^2 \qquad (3b)$$

Similarly, at points B and C in the solid curve in Fig. 4a the polarization combinations are all,p,p (α = 90°, β = 90°) and all,s,s (α = 0°, β = 0°), respectively. The SFG intensity at B and C can be given as:

$$I_{\mathrm{B}} \propto |\chi^{(2)}_{1.\mathrm{all,p,p}}/L|^2 = |\chi^{(2)}_{yyy}\cos\theta - \chi^{(2)}_{xyz}\sin\theta|^2 \qquad (3c)$$

$$I_{\mathrm{C}} \propto |\chi^{(2)}_{1.\mathrm{all,s,s}}/L|^2 = |\chi^{(2)}_{xxx}|^2 \qquad (3d)$$

For Fig. 4b the incident plane is parallel to the fiber axis similarly to the configuration in Fig. 3b. At points A', B', and C' in Fig. 4b the polarization combinations are all,p,p (α = 0°, β = 0°), all,s,p (α = 90°, β = 0°), and all,s,s (α = 0°, β = 90°), respectively, and the SFG intensity depends on the effective susceptibilities as:

$$I_{\mathrm{A}'} \propto |\chi^{(2)}_{2.\mathrm{all,p,p}}/L|^2 = |\chi^{(2)}_{xxx}\cos\theta - \chi^{(2)}_{yxz}\sin\theta|^2 \qquad (4a)$$

$$I_{\mathrm{B}'} \propto |\chi^{(2)}_{2.\mathrm{all,s,p}}/L|^2 = |-\chi^{(2)}_{yyx}\cos\theta + \chi^{(2)}_{xyz}\sin\theta|^2 \qquad (4b)$$

$$I_{\mathrm{C}'} \propto |\chi^{(2)}_{2.\mathrm{all,s,s}}/L|^2 = |-\chi^{(2)}_{yxy}|^2 \qquad (4c)$$

Here the subscript 2 indicates the configuration in the inset of Fig. 3b. As we found in Fig. 3, the visible electric field in the *y* direction gives minor contribution, and so $\chi^{(2)}_{2.\mathrm{all,s,p}}$ in Eq. 4b is small.

Equation 3d shows that the SFG intensity at point C of the dashed curve in Fig. 4a is contributed only by the $\chi^{(2)}_{xxx}$ component. Thus, $\chi^{(2)}_{xxx}$ is regarded as relatively small. Then Eq. 4a shows that the SFG intensity at A' in Fig. 4b is mainly contributed by the $\chi^{(2)}_{yxz}$ element. Equation 4c shows that the SFG intensity at point C' of the dashed curve in Fig. 4b is contributed only by the $-\chi^{(2)}_{yxy}$ element. Seeing that the SFG intensity is at a minimum at point C, we can say the $\chi^{(2)}_{yxy}$ component is also relatively small.

Summarizing the discussion just above, we can say that $\chi^{(2)}_{yxz}$ and $\chi^{(2)}_{zxy}$ are dominant chiral nonlinear susceptibility components while $\chi^{(2)}_{yxy}$ and $\chi^{(2)}_{zxz}$ are weak but finite nonlinear susceptibility components of the cellulose. This is consistent with the general understanding of the second-order optical nonlinearity of chiral materials.[25]

The maximum contrast of the SFG intensity from the cellulose fiber at the peak 2945 cm^{-1} can be estimated as 0.78 from Fig. 4a and 0.66 from Fig. 4b when rotating the visible polarization. Here the contrast in images is expressed by the Michelson contrast formula as $(I_{\mathrm{Max}} - I_{\mathrm{Min}})/(I_{\mathrm{Max}} + I_{\mathrm{Min}})$. I_{Max} and I_{Min} are maximum and minimum intensities, respectively. The contrasts for Figs. 4a and 4b are higher than the contrast of

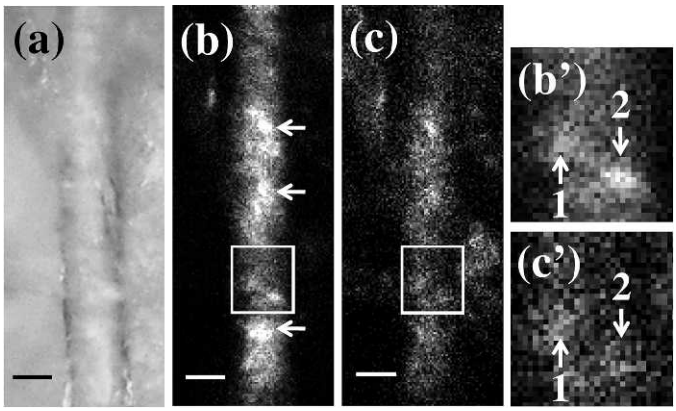

FIG. 5. (**a**) The linear CCD image of the cellulose fiber. SFG images of the cellulose fiber with (**b**) $\alpha = 0°$, $\beta = 90°$ and with (**c**) $\alpha = 90°$, $\beta = 90°$. The sensitivity of (c) was slightly increased for easier observation. The cellulose fiber was placed in a configuration similar to the inset in Fig. 3a. (**b'**) and (**c'**) are the expanded SFG image areas indicated by squares in (b) and (c), respectively. The scale bar is 10 μm.

0.29 in Raman data and the one of 0.30 in CARS data[14] at 2890 cm^{-1}.

Sum Frequency Images. Figure 5 shows a linear charge-coupled device (CCD) image (Fig. 5a) and four SFG images of the cellulose fiber with a diameter of about 17 μm at 2945 cm^{-1} in the same optical configuration as that in the inset in Fig. 3a. The polarization angles of the two input beams are (α, β) = (0°, 90°) for Figs. 5b and 5b' and (α, β) = (90°, 90°) for Figs. 5c and 5c'. The sensitivity of imaging for Figs. 5c and 5c' was slightly increased for easier observation. If we show the images of Figs. 5c and 5c' with the same sensitivity as those of Figs. 5b and 5b', we see no signal in the images in Figs. 5c and 5c'. Figures 5b' and 5c' are magnified images of the areas in the rectangular frames in Figs. 5b and 5c, respectively.

Since the SFG intensity in Fig. 5b is much stronger than that in Fig. 5c at almost all the positions of the fiber, we can say that molecular axes of the microfibrils tend to be oriented along the macroscopic fiber axis. However, the microscopic structure of the fiber is not found to be uniform when we see the SFG images more closely. There are very bright local spots in Fig. 5b. Some of the bright spots are indicated by arrows. The bright spots should be assigned to well-ordered domains with high crystallinity.[18] In Fig. 5b' the local spot indicated by arrow 2 is brighter than that indicated by arrow 1. On the other hand, in Fig. 5c' the local spot 1 is as bright as or even brighter than the local spot 2. We guess that variation of bunching and orientation of fibrils between different domains may be the cause of the different second-order nonlinear optical responses.

Figure 6 shows SFG images of another cellulose fiber when the fiber axis is parallel to the incident plane in the same optical configuration as that of the inset in Fig. 3b. The polarization of infrared light was kept in the incident plane and that of the visible light was set as parallel (Fig 6b; $\alpha = 0°$, $\beta = 0°$) and perpendicular (Fig.6c; $\alpha = 90°$, $\beta = 0°$) to the fiber axis. Figure 6b shows some bright local spots marked A on the fiber and they are dark in Fig. 6c. These local spots should be attributed to cellulose microfibril bunches well aligned along the fiber axis.

In the local spot B the SFG signal is weak in Fig. 6b, but relatively strong in Fig. 6c. This local area can be attributed to the bunching of fibrils with their axes nearly perpendicular to

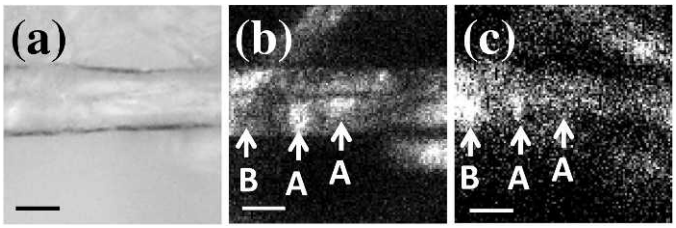

FIG. 6. (**a**) The linear CCD image of the cellulose fiber. SFG images of the cellulose fiber at 2945 cm^{-1} with (**b**) $\alpha = 0°$, $\beta = 0°$ and (**c**) $\alpha = 90°$, $\beta = 0°$. The sensitivity of image (c) was slightly increased for easier observation. The cellulose fiber was placed in a configuration similar to the inset in Fig. 3b. The scale bar is 10 μm.

the fiber axis. We can see a dark line near the center of the fiber in Fig. 6b, but not so clearly in the linear image in Fig. 6a and the SFG image in Fig. 6c. This dark center line is either a boundary between two fibers or a core area of a single fiber. If it is a boundary between two fibers, we should see it also in Fig. 6c. However, we do not see any centerlines in Fig. 6c. Thus, this line is probably a core area of a single fiber. Similar structures are reported in CARS microscopy images of cellulose fibers by Zimmerley and his co-workers.[14]

Figure 7 shows the dependence of the SFG image on the wavenumber of the infrared light. Figures 7b and 7c show the SFG images of another cellulose fiber at 2945 cm^{-1} and 2850 cm^{-1}, respectively. In Fig. 7b the local spot A is brighter than B, while in Fig. 7c the local spot A is as bright as the local spot B. In Fig. 7b a center dark line can be seen, while in Figs. 7a and 7c the center lines are not so clear.

As we see in Fig. 3 the SFG of the microfibrils are enhanced when the visible light is polarized parallel to the macroscopic fiber axis and the infrared wavenumber is in resonance with the vibration of the asymmetric CH_2 stretching mode at 2945 cm^{-1}. This is why the contrast of the SFG spots is higher in the fiber in Figs. 5b and 6b than in Figs. 5c and 6c and the center core line is clearer in Fig. 6b, as a response to the visible light polarization. The contrast of the SFG image is higher and the center line is clearer in Fig. 7b than in Fig. 7c, as a response to the infrared wavenumber. The core area observed in Fig. 6b and Fig. 7b can be either hollow or filled with different polysaccharides. Since the core area is not visible in the linear image of Fig. 7a, it may be some polysaccharide of different kinds from that of the outer cladding.

Figure 8a is a linear image of a cross section of a cellulose fiber, and Fig. 8b is a SFG image of the same fiber at 2945 cm^{-1}. The cross section is indicated by arrows in Figs. 8a and 8b. As we have already observed in Fig. 3, the SFG intensity is much weaker with the fiber axis parallel to the optical axis of

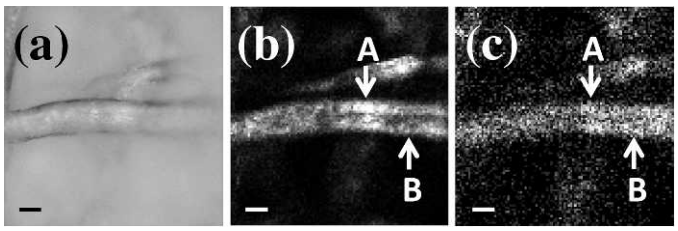

FIG. 7. (**a**) The linear CCD image of the cellulose fiber. SFG images of the cellulose fiber with $\alpha = 0°$ at (**b**) 2945 cm^{-1} and (**c**) 2850 cm^{-1}. The cellulose fiber was placed in a configuration similar to the inset in Fig. 3b. The scale bar is 10 μm.

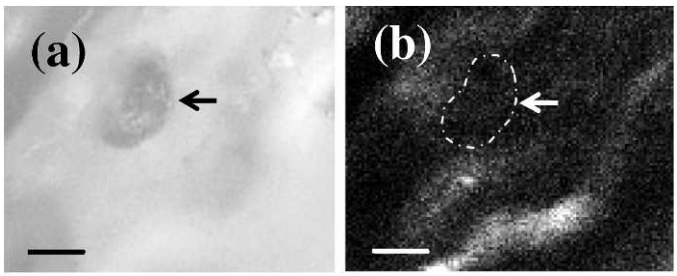

FIG. 8. (**a**) The linear image of the cross section of the cellulose fiber. (**b**) SFG images of the cellulose fiber at 2945 cm^{-1}. The cellulose fiber was placed in a configuration similar to the inset in Fig. 3c. The scale bar is 10 μm.

the collection optics than they are perpendicular to each other. Therefore, the SFG image of the cross section of the cellulose fiber looks darker than the surrounding fibers in Fig. 8b.

The observed domains of crystalline phase and their orientational ordering may indicate a cholesteric ordering of the cellulose microfibril bunches like liquid crystal molecules.[25] We have no further experimental evidence of such a state in our cellulose fibers, but it is suggested to be worth investigating further in the future.

CONCLUSION

This is the first SFG microscope study of cellulose fibers. The intensity of CH_2 asymmetric stretching modes at 2945 cm^{-1} and 2970 cm^{-1} depend strongly on the orientation of the cellulose microfibril bunches due to the chirality of crystalline cellulose at CH_2 groups. The second-order nonlinear susceptibility components $\chi^{(2)}_{yxz}$ and $\chi^{(2)}_{zxy}$ were found to be dominant. The orientation of microfibril bunches of the cellulose fiber was detected by SFG imaging with different polarization configurations or different resonant infrared wavelengths.

ACKNOWLEDGMENTS

We are grateful to Professor Masatoshi Osawa of Hokkaido University and Professor Tatsuo Kaneko from JAIST for their valuable comments and advice.

1. J. N. Gannaway and C. J. R. Sheppard, Opt. Quantum Electron. **10,** 435 (1978).
2. G. Cox, N. Moreno, and J. Feijo, J. Biomed. Opt. **10,** 204013 (2005).
3. G. Cox, E. Kable, A. Jones, I. Fraser, F. Manconi, and M. D. Gorrell, J. Struct. Biol. **141,** 53 (2003).
4. S.-W. Chu, I.-H. Chen, T.-M. Liu, P. C. Chen, and C.-K. Sun, Opt. Lett. **26,** 1909 (2001).
5. Y. Miyauchi, H. Sano, and G. Mizutani, J. Opt. Soc. Am. A **23,** 1687 (2006).
6. S. R. Walter and F. M. Geiger, J. Phys. Chem. Lett. **1,** 9 (2010).
7. Y. Sartenaer, G. Tourillon, L. Dreesen, D. Lis, A. A. Mani, P. A. Thiry, and A. Peremans, Biosens. Bioelectron. **22,** 2179 (2007).
8. L. Fu, J. Liu, and E. C. Y. Yan, J. Am. Chem. Soc. **133,** 8094 (2011).
9. J. Wang, X. Chen, M. L. Clarke, and Z. Chen, Proc. Natl. Acad. Sci. USA **102,** 4978 (2005).
10. P. Zugenmaier, *Crystalline Cellulose and Derivatives* (Springer, Berlin, 2008), p. 43.
11. Y. Nishiyama, P. Langan, and H. Chanzy, J. Am. Chem. Soc. **124,** 9074 (2002).
12. Y. Habibi, L. A. Lucia, and O. J. Rojas, Chem. Rev. **110,** 3479 (2010).
13. R. H. Atalla, R. E. Whitmore, and C. J. Heimbach, Macromolecules **13,** 1717 (1980).
14. M. Zimmerley, R. Younger, T. Valenton, D. C. Oertel, J. L. Ward, and E. O. Potma, J. Phys. Chem. B **114,** 10200 (2010).
15. N. Gierlinger, S. Luss, C. Koenig, J. Konnerth, M. Eder, and P. Fratzl, J. Exp. Bot. **61,** 587 (2010).
16. R. M. Brown, Jr., A. C. Millard, and P. J. Campagnola, Opt. Lett. **28,** 2207 (2003).
17. G. Mizutani and H. Sano, " Starch Image in Living Water Plants Observed by Optical Second Harmonic Microscopy", in *Science, Technology and Education of Microscopy: An Overview* (Microscopy Series No.1 Vol.2)**,** A. Mendez-Vilas, Eds. (FORMATEX, Badajoz, Spain, 2003), p. 499.
18. A. L. Barnette, L. C. Bradley, B. D. Veres, E. P. Schreiner, Y. B. Park, J. Park, S. Park, and S. H. Kim, Biomacromolecules **12,** 2434 (2011).
19. K. Locharoenrat, H. Sano, and G. Mizutani, Phys. Stat. Sol. C **6,** 304 (2009); Erratum ibid, **6,** 1345 (2009).
20. N. Ji, PhD thesis, University of California, Berkeley, Berkeley, California (2005).
21. R. W. Boyd, *Nonlinear Optics* (Academic Press, Boston, 1992), p. 44.
22. J. H. Wiley and R. H. Atalla, Carbohydr. Res. **160,** 113 (1987).
23. S. Fischer, K. Schenzel, K. Fischer, and W. Diepenbrock, Macromol. Symp. **223,** 41 (2005).
24. M. A. Belkin and Y. R. Shen, Int. Rev. Phys. Chem. **24,** 257 (2005).
25. R. Chiba, Y. Nishio, Y. Sato, M. Ohtaki, and Y. Miyashita, Biomacromolecules **7,** 3076 (2006).